Article:
Chen, Sidong, Paschalis, Stefanos orcid.org/0000-0002-9113-3778, Petri, Marina orcid.org/0000-0002-3740-6106 et al. (4 more authors) (2025) Development of the self-calibration technique for γ -ray energy tracking arrays. European Physical Journal A. 195. ISSN: 1434-601X

https://doi.org/10.1140/epja/s10050-025-01651-0

Eur. Phys. J. A manuscript No.
(will be inserted by the editor)

Development of the self-calibration technique for γ-ray energy tracking arrays

S. Chen[1,a], **S. Paschalis**[1,b], **M. Petri**[1], **M. A. Bentley**[1], **M. Labiche**[2], **S. Heil**[1], **F. Holloway**[3]

[1]School of Physics, Engineering and Technology, University of York, Heslington, York YO10 5DD, UK
[2]Science and Technology Facilities Council (STFC), Daresbury Laboratory, Keckwick Lane, Warrington, UK
[3]University of Liverpool, Oliver Lodge Building, L69 7ZE, Liverpool, UK

Received: date / Accepted: date

Abstract Determining the three-dimensional γ-ray interaction position in γ-ray tracking arrays is achieved by comparing in real time the measured electronic signals against a pre-generated library of calculated signals (signal basis) that maps the detector response throughout the crystal volume. Obtaining a high-fidelity signal basis remains a significant technological challenge that often limits the ulitmate performance of the arrays. To address this, a self-calibration method was proposed to generate the signal basis experimentally, in an iterative way and in situ; its potential has been demonstrated in a proof-of-concept study using a simplistic geometry. In this article, we extend and refine this innovative technique for γ-ray tracking arrays using realistic simulations of the actual crystal geometries and including pulse-shape analysis that mimics the reconstruction that takes place experimentally. Key factors determining the performance of the method, such as the conditions for position convergence, statistical requirements, the impact of convoluting electronic noise to the signals, and the time alignment are investigated systematically within this framework. The results show that the method is robust and holds promise for generating high-fidelity signal basis experimentally. The analysis framework established in this work sets the stage for applying the self-calibration technique to real experimental data.

Keywords γ-ray energy tracking array · AGATA · GRETA · position resolution · pulse-shape analysis

[a]e-mail: sidong.chen@york.ac.uk
[b]e-mail: stefanos.paschalis@york.ac.uk

1 Introduction

High precision γ-ray spectroscopy is one of the most powerful tools to study the structure and properties of the atomic nucleus. In the last two decades, the frontier of γ-ray spectroscopy has shifted towards the development of γ-ray tracking arrays based on highly segmented High Purity Germanium (HPGe) detectors [1–18]. Tracking alludes to the reconstruction of the γ-ray interaction sequence (and hence track) and enables one to resolve high-multiplicity (high-fold) events, reject background events and determine the direction of the incoming γ ray. The most advanced implementation of this technique is being materialised in two arrays: the Advanced Gamma Tracking Array (AGATA) [19] in Europe and the Gamma Ray Energy Tracking Array (GRETA) [20–23] in the USA. The tracking performance of these arrays relies heavily on the precise determination of the γ-ray interaction position within the detector volume and the fraction of deposited energy in each interaction. This is realised by comparing in real time the position sensitive experimental signals against a pre-generated library of calculated signals (signal basis) that maps the detector response at different interaction positions within the crystal volume. Obtaining a high-fidelity signal basis, however, remains a technological challenge and the position sensitivity suggested by [1] has not been reached with the current basis.

A novel method to generate a reliable signal basis, called hereafter the self-calibration method, has been proposed [24], enabling the γ-ray tracking devices to perform a self-calibration of their position sensitive response in situ, opening up the way for reaching their optimum performance. In the self-calibration method, a radioactive source is used to illuminate the whole array in situ, as shown in Figs. 1 and 2, and the detector

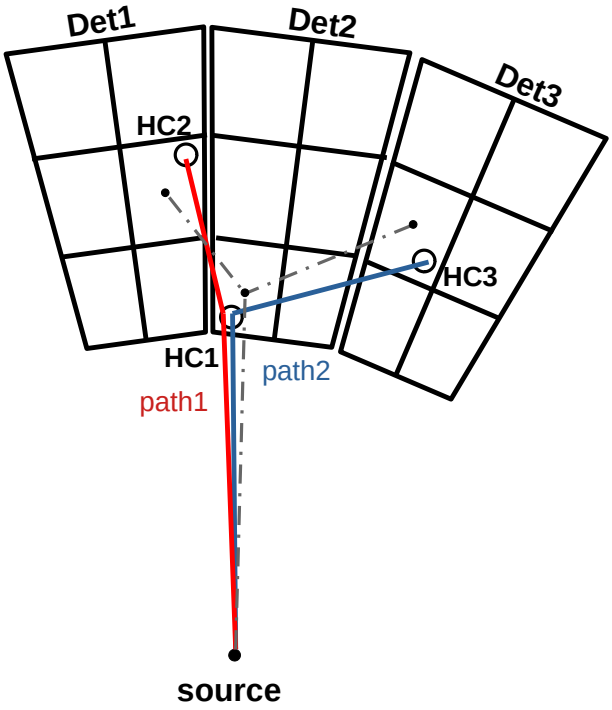

Fig. 1 Schematic representation of the Compton scattering events with segmented detectors for self-calibration analysis. Interactions from different events are grouped into collections referred to as *hit collections* (HCs). Paths, consisting of consecutive interactions, connect the HCs.

signals from Compton scattering events are recorded. Starting from the assumption of segment-size position resolution for all signals, and using an iterative minimization procedure based on the Compton scattering formula, it is possible to improve the position assignment for signals and converge to their real positions after several iterations.

The proof of principle as demonstrated in Ref. [24] was carried out using a simplified spherical shell geometry and employing simulated γ-ray interaction positions directly, without considering the signal generation process and the subsequent pulse-shape analysis. In this article, we extend the work of [24] by:

- validating the self-calibration method using the exact AGATA crystal shape with a reasonable sensitive area, and the detailed array geometry in the Geant4 simulation;
- using realistic simulated electric pulses to evaluate the performance and robustness of the self-calibration technique.

As such, the current implementation constitutes an essential step in demonstrating the effectiveness of the method and provides a complete, realistic, end-to-end analysis system for the self-calibration method that can be adapted for use with experimental data, which will form the material of a subsequent publication.

More specifically, the advances of the present work include the following.

1. **AGATA geometry implementation**. In our simulation, the actual AGATA detector geometries are used. Every detector is divided into 36 segmentation areas: 6-fold sector-wise segmented through the middle of the flat hexagonal front side and 6-fold longitudinal segmented along the detector length, as shown in Figs. 4 and 5 of Ref. [19].
2. **Pulse-shape-analysis implementation**. While in the initial demonstration of the method [24], the γ-ray interactions were grouped within a certain region according to the interaction positions from the simulation and the expected signal sensitivity, this information is not directly accessible experimentally. Instead the grouping of interaction points can only be achieved by comparing the similarity of the recorded pulse shapes and, using this criterion, the interaction points are grouped to define a so-called hit collection. Therefore, realistic pulse-shape data are generated in our simulation and the entire analysis is performed starting from generated pulses in order to mimic the experimental analysis procedure as close as possible.

Following the grouping based on pulse shapes, we then apply the self-calibration method [24] and generate a signal basis. This generated signal basis is used and evaluated using the AGATA Pulse Shape Analysis (PSA) algorithm [25] to extract the interaction positions and, hence, validate the method and demonstrate its performance.

This paper presents the generation of simulation data in Sect. 2. The self-calibration analysis processes are detailed in Sect. 3, followed by the presentation of analysis results in Sect. 4. Sect. 5 discusses the impact of statistics, noise levels and time alignment. Finally, the outlook is provided in Sect. 6.

2 Simulated pulse-shape data

These simulated data are generated by combining the interaction information from the AGATA Geant4 simulation with the pulse shapes extracted from the AGATA Detector Library (ADL 3.0) [26].

2.1 Data reduction criteria

In this section we discuss the critical data reduction criteria, which constitutes an essential step in ensuring

that the simulated data are filtered in a realistic way that mimics the experimental data collection.

The ideal γ-ray events for applying the self-calibration technique involve at least one Compton scattering interaction and at least two interactions within the array, with single interactions occurring in each detector. Additionally, the energy deposited at each interaction point should be sufficiently large to ensure a high signal-to-noise ratio. Therefore, to acquire suitable data in real measurements, the following procedure would be employed:

1. Position a γ-ray source at a specific location to illuminate the detector array.
2. Apply a trigger condition that enhances the selection of Compton scattering events, such as requiring at least two detectors to record significant energy deposits (fold-2 trigger).
3. Record the pulse-shape data for all triggered detectors.

We replicate this process in the simulation to generate Compton scattering pulse-shape data under the same conditions.

An important point in this process is that in real measurements it is challenging to distinguish during data acquisition the events with multiple interactions within the same segment from those with single interactions only. Hence, to mimic this we also collect simulation events with multi-hit interactions in a given segment and use pulse-shape comparison to try and exclude these, as one would do experimentally.

2.2 Geant4 simulated data

The Compton scattering interaction information was generated using the standard AGATA simulation package [27, 28], which is based on the Geant4 toolkit [29, 30]. In this work, the simulated AGATA array consists of 15 AGATA triple clusters arranged in the 1π configuration, as shown in Fig. 2. The cryostats and the detector encapsulation were not included in the simulation. A point-like γ-ray source, emitting 2 MeV γ rays isotropically, was positioned at the centre of the array, 235 mm from the front face of the detectors. Each γ-ray emission was treated as an independent event. The simulation provided the position and energy deposition of every interaction point within the detectors. The total energy deposited in each detector was computed by summing the energies of all interactions within that detector. Detectors with a total energy deposit exceeding 300 keV were considered as triggered detectors, and their interaction information was recorded. To select Compton scattering events, at least two triggered detectors were required.

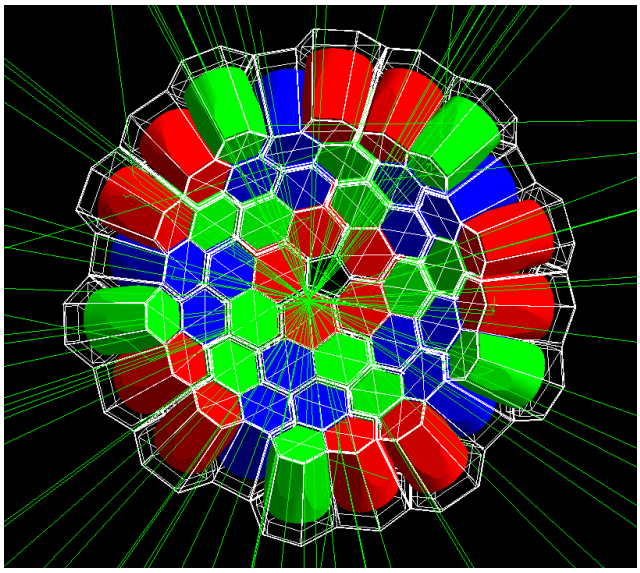

Fig. 2 Geometry of AGATA 1π configuration. Red, green, and blue colours represent A-, B-, and C-type crystals, respectively. A point-like γ-ray source is placed at the centre of the array, emitting 2 MeV γ rays (green lines).

A total of 1×10^{10} events were simulated, yielding 2.6×10^{8} events that met the selection criteria. The segments located on the back side of the crystals presented significantly lower statistics compared to those on the front side. To illuminate the array more efficiently and increase statistics for back-side segments, the point-like γ-ray source was also placed at two additional positions: 75 mm in front of and 75 mm behind the central detector. For each position, 5×10^{9} events were simulated. The useful data from all three source positions were combined to perform the self-calibration analysis.

2.3 Pulse-shape generation

To generate pulse shapes, the ideal approach would involve inputting the interaction data produced by Geant4 into the electric field calculation software designed for modeling segmented High-Purity Germanium detectors, such as ADL 3.0 [26] and AGATAGeFEM [31]. However, these calculations are computationally intensive and therefore not feasible for the large dataset required in this work. Furthermore, achieving the most accurate representation of the pulse shape is not essential for the purposes of this study. Instead, a more efficient method, involving the linear interpolation of pre-generated signal bases, is employed to produce the pulse shapes. For each interaction point, the pulse shape response is determined by performing trilinear interpolation of the

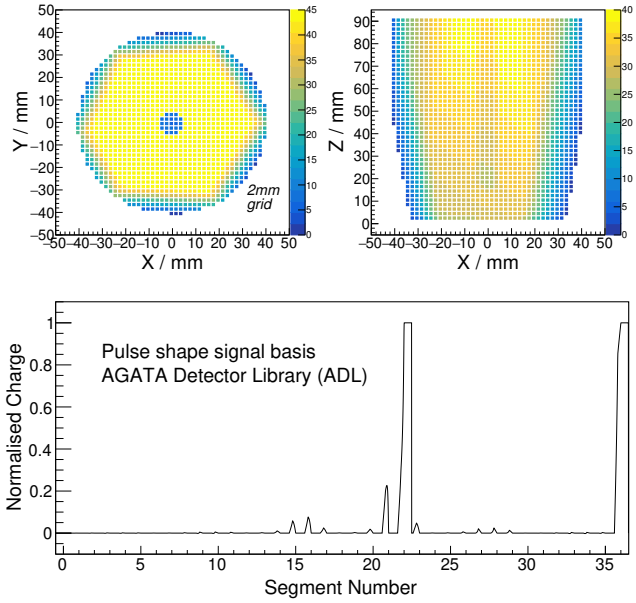

Fig. 3 AGATA Detector Library (ADL) signal basis. The upper panels show the positions of the grid points projected onto the XY and XZ planes. The colour code indicates the number of grid points in each projection. The lower panel shows an example of the pulse shape in signal basis. The interaction is in segment 22 in this example. The core signal is assigned to ID 36.

ADL signal basis, which is calculated on a 2 mm grid. Fig. 3 illustrates the spatial distribution of the ADL signal basis for an A-type crystal, along with an example of a representative pulse shape.

Since pulse shapes vary significantly depending on the segment where the interaction occurs, only the signal bases of the grid points within the same segment as the interaction are used for interpolation. When an interaction occurs in the inner part of a segment, the eight grid points closest to the interaction form a cube that surrounds the interaction point, and the interpolation is performed using the signal bases of these eight grid points. For interactions near the edges of a segment, where grid points may lie only on one side of the interaction, extrapolation is employed to generate the pulse shape. The pulse shape responses from all interactions within one detector are summed for each event, producing the simulated pulse-shape data.

To simulate experimental data as realistically as possible, the preamplifer response and cross-talk response are applied to the signal basis, and noise – primarily originating from electronic circuits – is convoluted into the simulated signal. Artificial noise is generated with a frequency distribution similar to the noise observed in actual experiments. This noise affects the self-calibration process mainly in the grouping of pulse shapes. However, its impact can be mitigated by selecting only signals with large energy deposition, although this approach results in a reduction in statistics. For the initial validation of the self-calibration method, noise is excluded to simplify the analysis. Subsequently, a noise level of 3 keV (RMS) is introduced into the signals to evaluate its impact on the method and to develop an effective grouping method suitable for real experimental data.

3 Self-Calibration Analysis

The self-calibration analysis, which is designed to apply to both simulated and experimental data, is conducted in two stages. In the first step, pulse shapes from different events are grouped into collections referred to as *hit collections* (HCs). For each HC, an average pulse shape is calculated, and its position is initially assigned to the geometric centre of the corresponding segment. In the second step, the position assignments of the HCs are refined through iterative optimisation based on a figure-of-merit (FOM) derived from the Compton scattering formula. This optimisation process requires several iterations to achieve convergence and ensure accurate results (as described in Ref. [24]).

3.1 Grouping pulse shapes

In the study of Ref. [24], the grouping of γ-ray interaction points (referred to as *hits*) was based on their simulated positions. Spherical hit collections (HCs) of uniform geometrical sizes were generated across the detectors, with their diameters being well controlled. In experimental scenarios, however, grouping achieved through pulse shape comparison cannot produce HCs with such consistent and well-defined geometrical properties. Due to the varying sensitivity of pulse shapes across the crystal volume, the resulting HCs exhibit irregular shapes and inconsistent sizes. A crucial aspect of this work is to investigate whether the self-calibration method remains effective when applied to these realistic non-uniform HCs.

An example of comparing two pulse shapes is illustrated in Fig. 4. Both pulse shapes are normalised, with their core amplitudes scaled to unity. These pulse shapes are characterised by prominent net-charge signals in the direct-hit segment (segment 20 in this case) and the core, and small reflection signals in neighbouring segments. To quantitatively compare the two pulse shapes, the χ^2 differences, defined as the absolute values of the differences, are calculated for each signal point and plotted in the upper panel, alongside the summed χ^2 differences for each segment and the core.

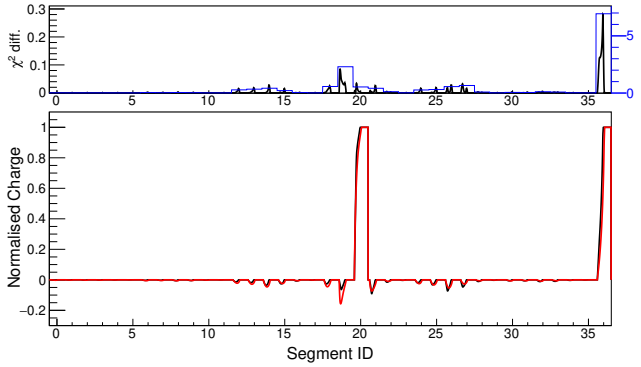

Fig. 4 Comparison of two pulse shapes. The amplitudes of the pulse shapes are normalised to 1 before comparison. The upper panel shows the χ^2 differences between two pulse shapes (black), and the sum of the χ^2 differences in every segment and the core (blue). The 36 segments are assigned segment ID from 0 to 35. The core signal is assigned to "segment ID" 36.

The interaction position within the detector is typically described using cylindrical coordinates: radial r, azimuthal ϕ and longitudinal z. Despite the complex relationship between interaction position and pulse shape in AGATA detectors, empirical observations indicate specific correlations:

- The position along the radial direction is reflected in the steepness of the rising edge of signals in the direct-hit (net charge) segment (segment 20 in this case) and the core.
- The position in the ϕ direction, defined as $r \times \phi$, is best seen from the amplitudes of reflection signals in neighbouring segments within the same slice (segment 14 and 26 in this case).
- The position along the longitudinal direction is inferred from the amplitudes of reflection signals in neighbouring segments within the same sector (segment 19 and 21 in this case).

Based on this understanding, three separate χ^2 metrics are calculated to characterise the positional differences:

- χ_0^2, summing the χ^2 values for the direct-hit segment and the core,
- χ_1^2, summing the χ^2 values for neighbouring segments within the same slice, and,
- χ_2^2, summing the χ^2 values for neighbouring segments within the same sector.

In cases where the direct-hit segment is the foremost or rearmost segment, χ_2^2 sums contributions from the nearest and next-to-nearest neighbouring segments.

The correlations between the three χ^2 metrics and the interaction distances along their corresponding directions are shown in Fig. 5. Radial and longitudinal distances are well constrained by applying cuts to χ_0^2 and χ_2^2, as illustrated in Fig. 5(b) and (d), respectively. However, defining an effective cut for χ_1^2 is more challenging, as shown in Fig. 5(c). The specific χ^2 conditions applied to form HCs are $\chi_0^2 < 2$, $\chi_1^2 < 0.1$ and $\chi_2^2 < 1$. The resulting distance distribution, between interactions within HCs, under these conditions is displayed in Fig. 5(a) in red colour.

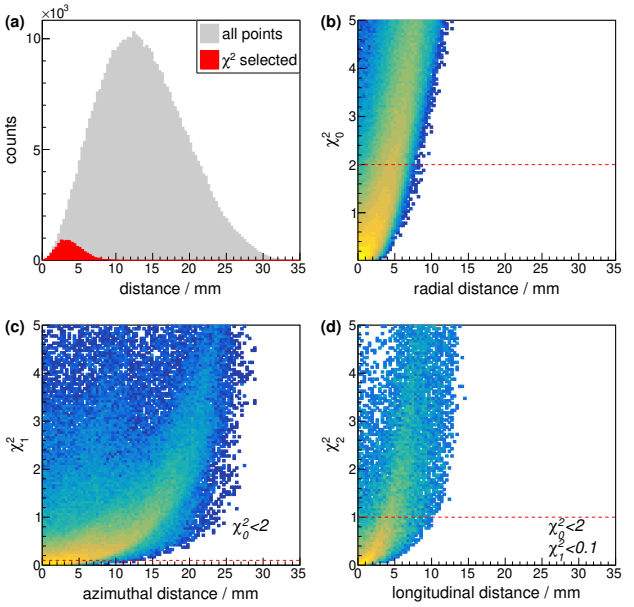

Fig. 5 Grouping pulse shapes with χ^2 conditions. (a) distance between interactions in one AGATA segment (ID=2). The red part is selected with χ^2 conditions: $\chi_0^2 < 2$, $\chi_1^2 < 0.1$ and $\chi_2^2 < 1$. (b) χ_0^2 vs. radial distance between interactions in segment 2. (c) χ_1^2 vs. azimuthal distance, with the condition $\chi_0^2 < 2$. (d) χ_2^2 vs. longitudinal distance, with the conditions $\chi_0^2 < 2$ and $\chi_1^2 < 0.1$. The red dashed lines in (b), (c)and (d) shows the χ^2 cuts.

The grouping of pulse shapes follows the following procedure: Each hit, characterised by its pulse shape, is compared to the representative pulse shape of existing hit collections (HCs). If the differences meet the specified χ^2 criteria, the hit is assigned to the respective HC. This comparison is repeated for all existing HCs, allowing a hit to be assigned to multiple HCs. Hits that cannot be assigned to any HC are used to define new HCs, with their pulse shapes serving as the representative pulse shapes for the newly formed HCs. Once all hits in the dataset have been processed, any HC containing more than 400 hits is further subdivided using stricter χ^2 conditions. This subdivision minimises the spacial spread of HCs and increases their density within the detector volume.

3.2 Position Optimisation

Following the grouping of pulse shapes, the average pulse shape is calculated for every hit collection (HC). Initially, all HCs are assigned to the respective segment centres. The subsequent step involves determining the optimal centre positions for these HCs. This is achieved through a position optimisation procedure.

To perform position optimisation, it is necessary to first track the sequence of interactions in each event. For this purpose, the Orsay forward-tracking algorithm (OFT) [23, 32] is employed. This algorithm is adapted to take advantage of the known γ-ray source position and the incident γ-ray energy, enabling the tracking to initiate from the source position. The position of a hit is calculated as the average position of the HCs to which the hit is assigned, which corresponds to the segment centre at the beginning of the process. Once the HC positions are optimised, the tracking process can be repeated for improved accuracy. After tracking, the hits in an event are sequenced to form a track. The source position is designated as the starting point for the track. For each subsequent hit, the position, energy deposit, and incident γ-ray energy are recorded. The incident energy is determined by subtracting the energy deposits of preceding hits from the initial γ-ray energy. A track is further divided into subsets called paths, consisting of three consecutive hits. These paths represent the minimum set required to compare the geometrical scattering angle with the Compton scattering angle. The geometrical angle is derived from the hit positions within the path, and it is directly influenced by the HC position assignments. The Compton scattering angle is calculated using the following formula:

$$\cos(\theta) = 1 + \frac{m_e c^2}{E_{inc}} - \frac{m_e c^2}{E_{inc} - E_{dep}}$$

where E_{inc} is the incident γ-ray energy, and E_{dep} is the energy deposit at the middle hit of the path.

The HCs are interconnected through numerous paths. The discrepancies between the geometrical angles and Compton scattering angles from all paths linked to a given HC are aggregated to calculate the figure-of-merit (FOM) for that HC. During the optimisation process, the positions of the HCs are iteratively adjusted to minimise their respective FOM values. In practice, the position optimisation is performed one HC at a time, while keeping the positions of all other HCs fixed. This process is iterated over all HCs, and the entire procedure is repeated using the updated HC positions. Several iterations are required to achieve convergence. To prevent extreme position shifts caused by poor initial position assignments, the position adjustments for each interaction are restricted to a maximum of 5 mm in any direction. Additionally, movements across segment boundaries are penalised by assigning large FOM values, thereby ensuring that HCs remain within their original segment.

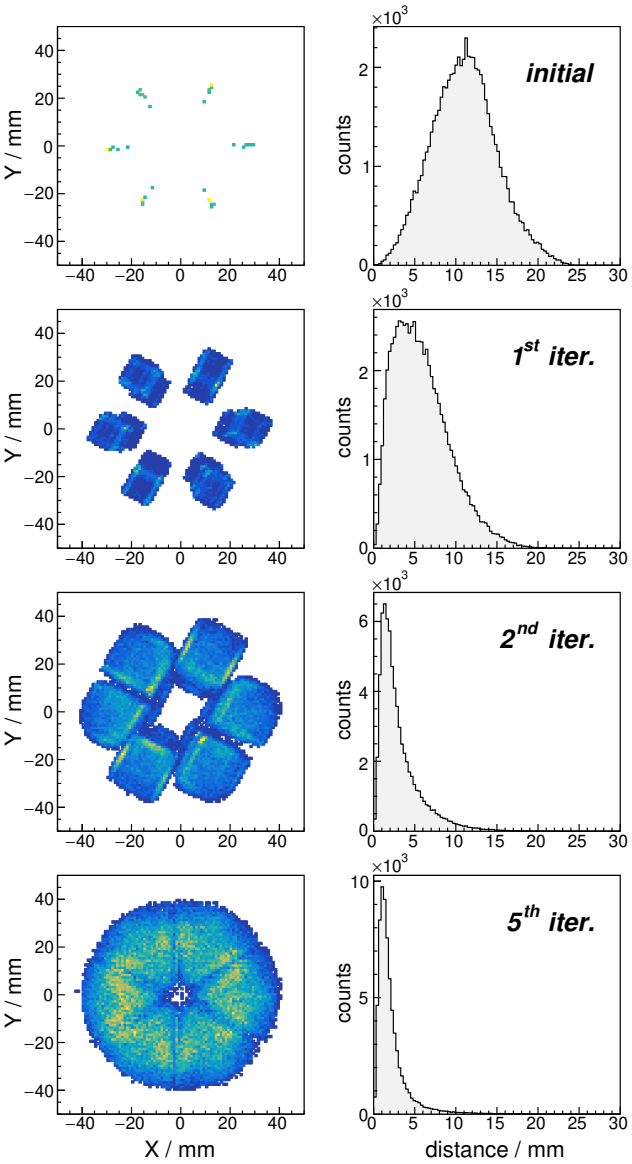

Fig. 6 Hit Collections (HCs) position optimisation. The plots on the left show the position distribution of the HCs in XY-plane. The plots on the right show the distance between the assigned position and the real position of the HCs.

The progression of the position optimisation for a single detector is illustrated in Fig. 6. Initially, HCs are only assigned to the segment centres, resulting in 36 discrete points in the XY-plot. The initial distances between the assigned HC positions and the true positions exhibit a broad distribution, peaking around 12 mm. As the optimisation progresses, the HC positions gradually spread across the detector volume, with the distance

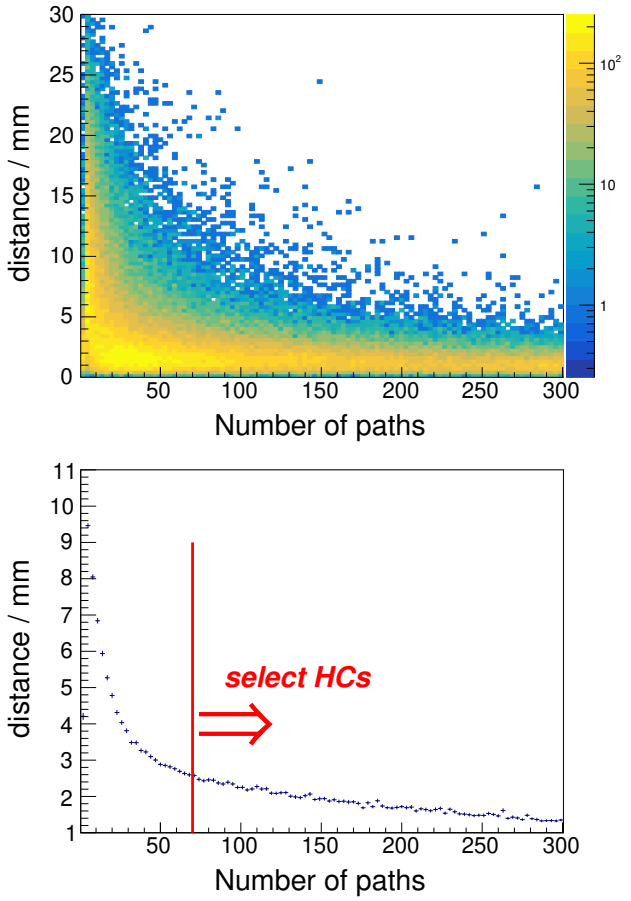

Fig. 7 Hit Collections (HCs) position convergence versus the number of paths. The upper panel shows the 2D-distribution for all HCs, and the lower panel shows the profile.

distribution narrowing and peaking at approximately 2 mm. This reduction in distances indicates the convergence of HC positions.

3.3 Position Convergence

The convergence of HC positions is strongly influenced by the number of paths connected to each HC. Fig. 7 illustrates the relationship between the final position offsets and the number of paths associated with each HC. HCs connected to only a few paths exhibit broader position distributions, with average deviations reaching up to 10 mm. In contrast, HCs connected to a higher number of paths converge more closely to their true positions, making them suitable candidates for constructing the signal basis for PSA. In experimental scenarios, these position offsets cannot be determined since the true positions are unknown. However, this simulation study demonstrates that selecting HCs based on their path count can effectively enhance position accuracy.

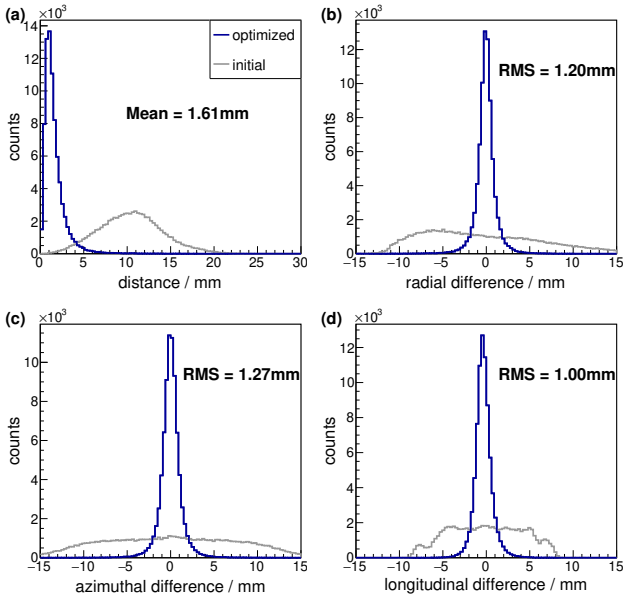

Fig. 8 Difference between the assigned position and the real position of the selected hit collections (HCs). (a) difference in distance. (b) difference in radial direction. (c) difference in azimuthal direction. (d) difference in longitudinal direction. The gray histograms show position difference from the initial HC position assignments (segment centre), and the blue histograms show position difference after optimisation.

For this study, HCs with more than 70 paths are designated as "good HCs" and used to construct the signal basis. The position convergence of these selected HCs, along with their positional differences in the radial (r), azimuthal (ϕ), and longitudinal (z) directions, is shown in Fig. 8. The deviations in the ϕ direction are slightly larger than those in the r and z directions, likely due to the reduced sensitivity of pulse shapes to variations in the ϕ direction.

4 Self-Calibration Results

The self-calibration signal basis is constructed from the selected hit collections (HCs), using their averaged pulse shapes and assigning them to their converged positions. To assess the quality of the generated basis, two evaluation methods are employed: direct pulse-shape comparison and PSA performance evaluation.

4.1 Fidelity of self-calibration signal basis

Since the pulse shape data was generated from the ADL basis, the ADL basis serves as the reference for the most accurate signal representation in this study. The fidelity of the self-calibration basis is evaluated by comparing

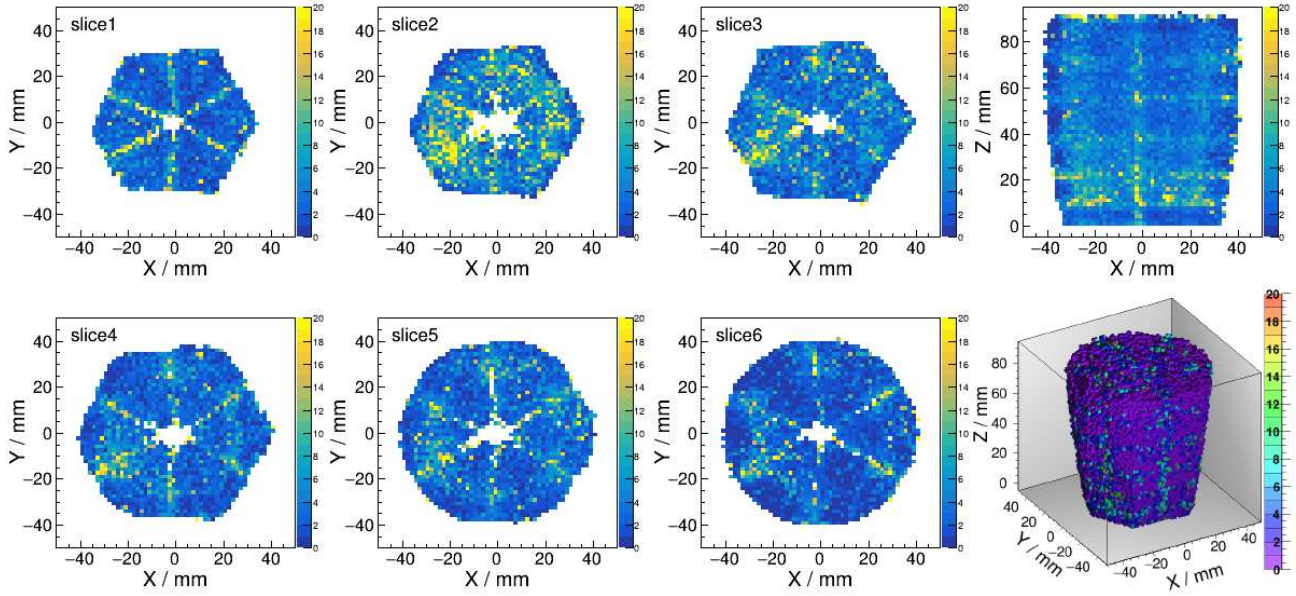

Fig. 9 The χ^2 differences between the pulse shapes in the self-calibration basis and the ADL basis.

it directly to the ADL basis at corresponding interaction positions. This comparison provides a global view of the self-calibration basis and highlights problematic areas with large deviations from the original basis. For each selected hit collection (HC), the total χ^2 differences are calculated between the pulse shapes in the self-calibration basis and the ADL basis. The results are presented in Fig. 9. The comparison is visualised in 2D plots, where each slice of the detector is represented in the XY-plane, and the entire detector is represented in the XZ-plane. A 3D plot is also presented.

In the 2D plots of Fig. 9, blue regions indicate areas with small total χ^2 differences, signifying high-fidelity signal bases derived from the self-calibration method. Conversely, yellow regions represent areas with large χ^2 differences, highlighting discrepancies between the self-calibration and ADL pulse shapes. The regions with large χ^2 values are predominantly near the segment boundaries. This is attributed to the rapid signal shape variations in these regions, which challenge the grouping of pulses and the formation of sufficiently populated HCs. Consequently, the converged positions and the averaged pulse shapes in these regions tend to deviate more significantly from their real values. This limitation could be mitigated in the future by increasing statistics, as discussed in Sect. 5.1. The segments in the second slice (slice2) contain more yellow points compared to those in other slices. This is due to the second slice being thinner than the others and having a larger boundary area, as illustrated in Fig. 2 of Ref. [33].

4.2 Pulse-Shape Analysis with self-calibration basis

To quantitatively evaluate the self-calibration basis, the second method involves using it in pulse-shape analysis (PSA) to determine interaction positions and comparing the deduced positions to the simulated ones. The position differences in the ϕ, r and z directions, representing the PSA position resolution in each direction, are shown in Fig. 10 for the ADL basis (a) and the self-calibration basis (b). When using the ADL basis for PSA, position resolutions of approximately 2 mm (FWHM) are observed in all three directions, as expected given the granularity of the ADL basis. For the PSA using self-calibration basis, the position resolutions are approximately 3 mm (FWHM), notably good comparing with the position resolutions achieved with experimental data [18, 33, 34]. This highlights the potential of the self-calibration basis to significantly improve the position resolution in experimental applications.

5 Discussion

Using the simulation data, we successfully demonstrated the feasibility of the self-calibration method when applied to pulse-shape data with the AGATA detector geometry. However, three critical aspects must be addressed for practical implementation with real experimental data: statistics, noise and time alignment.

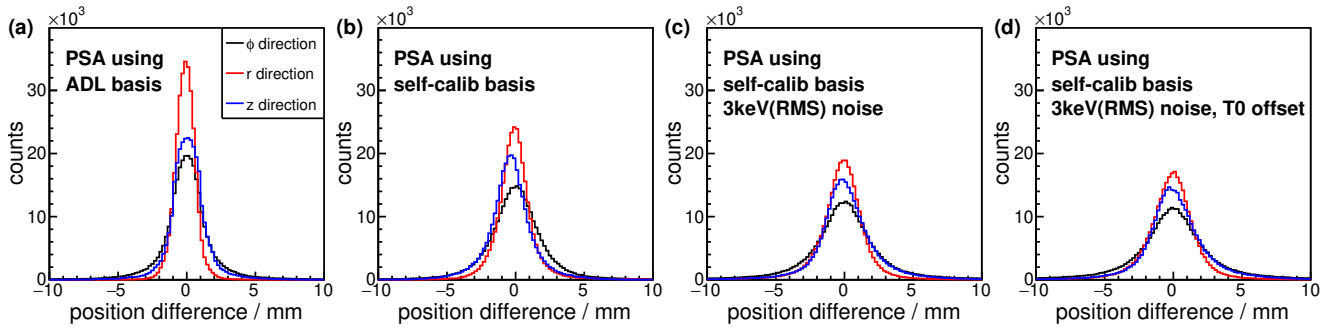

Fig. 10 Position resolution from PSA using (a) the ADL basis; (b) the self-calibration basis; (c) the self-calibration basis generated from signal data including 3 keV (RMS) noise. (d) the self-calibration basis generated from signal data including 3 keV (RMS) noise and T_0 offset.

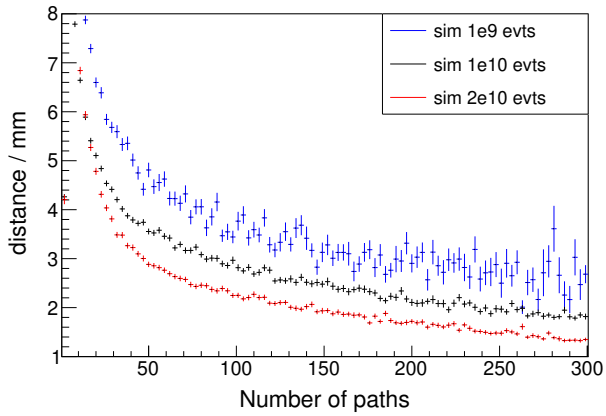

Fig. 11 Hit collections position convergence with different statistics.

5.1 Influence of statistics

The self-calibration method heavily relies on high statistics, particularly for grouping pulse shapes near the segment boundaries. Higher statistics allow the use of stricter χ^2 conditions to refine the pulse shapes within hit collections and facilitate connections to more "good" hit collections – those whose positions will converge to their actual positions during the optimisation process. Fig. 11 demonstrates the impact of statistics on position convergence. As the statistics increase, hit collections associated with the same number of paths achieve shorter convergence distances.

In a real experiment, the 2×10^{10} events used in the simulation could be generated with a 500 kBq source over approximately 12 hours. However, experimental constraints, such as signal pile-up, result in partial data loss and suggest extending the data acquisition period – by a factor of 10 – as a feasible approach to obtain high-quality data comparable to the simulated one.

5.2 Influence of noise

Electronic noise in pulse shapes primarily affects the analysis in two ways: it increases the absolute values of the χ^2 differences and smears the χ^2-distance correlations in Fig. 5. Consequently, the χ^2 conditions optimised for analysing noise-free simulation data are not directly applicable to data containing noise or real experimental data. The smearing of χ^2-distance correlations further complicates the establishment of predefined χ^2 conditions for grouping pulse shapes as shown in Fig. 5.

To address these challenges, a grouping method with dynamic χ^2 conditions was developed. In this approach, predefined χ^2 conditions are replaced with a procedure where only the maximum number of hits allowed in a hit collection is specified initially. All pulse shapes within the same segment are initially grouped into a single large hit collection, and the averaged pulse shapes for each hit collection is calculated. Each pulse shape is then compared to the averaged pulse shape to evaluate its deviation. The distributions of these deviations are used to dynamically generate χ^2 conditions, which are applied to divide the hit collection. This process is iteratively performed for all hit collections exceeding the predefined maximum hit number.

In this study, a noise level of 3 keV (RMS) was added to the signals, which is consistent with experimental observations. The pulse shape grouping method described above was applied to the noisy signal data, with a maximum hit number set to 400. The entire self-calibration analysis was then repeated on this dataset to generate a self-calibration basis, which was subsequently used in the PSA analysis. Fig. 10(c) shows the position resolution from PSA using this self-calibration basis. Position resolutions of approximately 3.5 mm (FWHM) are obtained, which remain competitive to achieve an improved resolution.

Since the χ^2 conditions are generated dynamically based on the data itself, this method is adaptable and resilient to varying noise levels and is also suitable for real experimental data. The optimized maximum hit number depends on the available statistics and can be determined using simulation data.

5.3 Time alignment

In real experimental data, signal traces are recorded upon the generation of triggers, which are derived from the core-contact pulses using either a constant fraction discriminator (CFD) or a leading-edge discriminator (LED). Due to electronic noise and variations in pulse shapes and amplitudes, the trigger signals can occur at different time relative to the onset of the core-contact pulse. This introduces a timing uncertainty, commonly referred to as the T_0 offset, in the recorded traces. Consequently, time alignment is required before the comparison of traces from experimental data. This effect was also studied using the simulation data to better understand its impact and guide the alignment procedure.

In this study, the trigger time for each simulated event was determined using a CFD applied to the core-contact pulse. The simulated traces were then time-shifted to align the trigger time across different events. This procedure mimics the data acquisition process of the AGATA front-end electronics, therefore making the simulation data more representative of real experimental conditions. For the self-calibration analysis of data affected by T_0 offset, a T_0 fitting procedure was implemented. This involved applying a relative time shift between two traces to minimise the χ^2 value in the pulse-shape comparison. Fig. 10(d) shows the position resolution obtained from PSA using the self-calibration basis with 3 keV (RMS) noise and T_0 offset. Including the T_0 offset introduces only a marginal degradation in resolution compared to the case without T_0 offset, as shown in Figs. 10(c) and (d), confirming the capability of the self-calibration technique to generate a high-fidelity signal basis experimentally.

6 Outlook

The self-calibration analysis package developed in this study for simulation data will be adapted to process experimental data by incorporating compatibility with the experimental data format. Experimental data will be collected using an intense ^{88}Y source ($\sim$500 kBq) with the AGATA array at INFN Legnaro National Laboratory (LNL), Italy. The ^{88}Y source emits γ-rays at two distinct energies, 898 keV and 1836 keV. Both of these energies can produce Compton scattering events with significant energy deposits, making them suitable for self-calibration analysis.

In this analysis, it is essential to identify the incident γ-ray energy for each event. This can be achieved during the tracking process by comparing the figure-of-merit (FOM) values for the two possible incident energy assumptions. A test using simulated ^{88}Y data demonstrated this capability. By assigning segment centre positions to all interactions, the OFT tracking algorithm successfully identified the correct incident γ-ray energy with an accuracy exceeding 96%. This high accuracy is attributed to the well-separated energies of the two γ rays and the spatially distinct interactions selected for self-calibration. These factors enable reliable tracking performance, even when the initial interaction positions are determined with segment-size resolution.

The self-calibration basis generated from the experimental data will then be applied to the pulse-shape analysis (PSA) of a benchmark in-beam γ-ray experiment. The results obtained using the self-calibration basis will be compared with those derived using the ADL basis to evaluate the effectiveness and performance improvements offered by the self-calibration approach.

Acknowledgements This work is supported by the UKRI Science and Technology Facilities Council under grant numbers ST/T003480/1, ST/T000546/1, ST/V001035/1, ST/Y000285/1, and the Royal Society.

References

1. K. Vetter, A. Kuhn, M. Deleplanque, I. Lee, F. Stephens, G. Schmid, D. Beckedahl, J. Blair, R. Clark, M. Cromaz, R. Diamond, P. Fallon, G. Lane, J. Kammeraad, A. Macchiavelli, C. Svensson, Nucl. Instrum. Methods Phys. Res., Sect. A **452**(1), 223 (2000). DOI https://doi.org/10.1016/S0168-9002(00)00430-7. URL https://www.sciencedirect.com/science/article/pii/S0168900200004307
2. K. Vetter, A. Kuhn, I. Lee, R. Clark, M. Cromaz, M. Deleplanque, R. Diamond, P. Fallon, G. Lane, A. Macchiavelli, M. Maier, F. Stephens, C. Svensson, H. Yaver, Nucl. Instrum. Methods Phys. Res., Sect. A **452**(1), 105 (2000). DOI https://doi.org/10.1016/S0168-9002(00)00431-9. URL https://www.sciencedirect.com/science/article/pii/S0168900200004319
3. I.Y. Lee, M.A. Deleplanque, K. Vetter, Rep. Prog. Phys. **66**(7), 1095 (2003). DOI 10.1088/0034-4885/

66/7/201. URL https://dx.doi.org/10.1088/0034-4885/66/7/201

4. M. Descovich, I. Lee, P. Luke, R. Clark, M. Cromaz, M. Deleplanque, R. Diamond, P. Fallon, A. Macchiavelli, E. Rodriguez-Vieitez, F. Stephens, D. Ward, Nucl. Instrum. Methods Phys. Res., Sect. A **545**(1), 199 (2005). DOI https://doi.org/10.1016/j.nima.2005.01.308. URL https://www.sciencedirect.com/science/article/pii/S0168900205004985
5. M. Descovich, I. Lee, M. Cromaz, R. Clark, M. Deleplanque, R. Diamond, P. Fallon, A. Macchiavelli, E. Rodriguez-Vieitez, F. Stephens, D. Ward, Nucl. Instrum. Methods Phys. Res., Sect. B **241**(1), 931 (2005). DOI https://doi.org/10.1016/j.nimb.2005.07.150. URL https://www.sciencedirect.com/science/article/pii/S0168583X05013546. The Application of Accelerators in Research and Industry
6. A. Boston, H. Boston, J. Cresswell, M. Dimmock, L. Nelson, P. Nolan, S. Rigby, I. Lazarus, J. Simpson, P. Medina, C. Santos, C. Parisel, Nucl. Instrum. Methods Phys. Res., Sect. B **261**(1), 1098 (2007). DOI https://doi.org/10.1016/j.nimb.2007.04.305. URL https://www.sciencedirect.com/science/article/pii/S0168583X07010270. The Application of Accelerators in Research and Industry
7. M. Cromaz, V. Riot, P. Fallon, S. Gros, B. Holmes, I. Lee, A. Macchiavelli, C. Vu, H. Yaver, S. Zimmermann, Nucl. Instrum. Methods Phys. Res., Sect. A **597**(2), 233 (2008). DOI https://doi.org/10.1016/j.nima.2008.07.137. URL https://www.sciencedirect.com/science/article/pii/S0168900208010942
8. F. Crespi, F. Camera, B. Million, M. Sassi, O. Wieland, A. Bracco, Nucl. Instrum. Methods Phys. Res., Sect. A **593**(3), 440 (2008). DOI https://doi.org/10.1016/j.nima.2008.05.057. URL https://www.sciencedirect.com/science/article/pii/S0168900208007821
9. J. Eberth, J. Simpson, Progress in Particle and Nuclear Physics **60**(2), 283 (2008). DOI https://doi.org/10.1016/j.ppnp.2007.09.001. URL https://www.sciencedirect.com/science/article/pii/S0146641007000828
10. J. Anderson, R. Brito, D. Doering, T. Hayden, B. Holmes, J. Joseph, H. Yaver, S. Zimmermann, IEEE Transactions on Nuclear Science **56**(1), 258 (2009). DOI 10.1109/TNS.2008.2009444
11. T. Ross, C. Beausang, I. Lee, A. Macchiavelli, S. Gros, M. Cromaz, R. Clark, P. Fallon, H. Jeppesen, J. Allmond, Nucl. Instrum. Methods Phys. Res., Sect. A **606**(3), 533 (2009). DOI https://doi.org/10.1016/j.nima.2009.04.024. URL https://www.sciencedirect.com/science/article/pii/S0168900209008250
12. N. Goel, C. Domingo-Pardo, T. Engert, J. Gerl, I. Kojouharov, H. Schaffner, Nucl. Instrum. Methods Phys. Res., Sect. A **652**(1), 591 (2011). DOI https://doi.org/10.1016/j.nima.2011.01.146. URL https://www.sciencedirect.com/science/article/pii/S0168900211002488. Symposium on Radiation Measurements and Applications (SORMA) XII 2010
13. C. Domingo-Pardo, N. Goel, T. Engert, J. Gerl, I. Kojouharov, H. Schaffner, F. Didierjean, G. Duchêne, M. Sigward, Nucl. Instrum. Methods Phys. Res., Sect. A **643**(1), 79 (2011). DOI https://doi.org/10.1016/j.nima.2011.04.021. URL https://www.sciencedirect.com/science/article/pii/S0168900211007595
14. S. Zimmermann, J.T. Anderson, D. Doering, J. Joseph, C. Lionberger, T. Stezelberger, H. Yaver, IEEE Transactions on Nuclear Science **59**(5), 2494 (2012). DOI 10.1109/TNS.2012.2205587
15. N. Goel, C. Domingo-Pardo, T. Habermann, F. Ameil, T. Engert, J. Gerl, I. Kojouharov, J. Maruhn, N. Pietralla, H. Schaffner, Nucl. Instrum. Methods Phys. Res., Sect. A **700**, 10 (2013). DOI https://doi.org/10.1016/j.nima.2012.10.028. URL https://www.sciencedirect.com/science/article/pii/S0168900212011606
16. P. Désesquelles, A. Boston, H. Boston, J. Cresswell, M. Dimmock, I. Lazarus, J. Ljungvall, L. Nelson, D.T. Nga, P. Nolan, S. Rigby, J. Simpson, N.T. Van-Oanh, Nucl. Instrum. Methods Phys. Res., Sect. A **729**, 198 (2013). DOI https://doi.org/10.1016/j.nima.2013.07.026. URL https://www.sciencedirect.com/science/article/pii/S0168900213010024
17. F. Crespi, et al., Nucl. Instrum. Methods Phys. Res., Sect. A **705**, 47 (2013). DOI https://doi.org/10.1016/j.nima.2012.12.084. URL https://www.sciencedirect.com/science/article/pii/S0168900212016324
18. P.A. Söderström, F. Recchia, J. Nyberg, A. Al-Adili, A. Ataç, S. Aydin, D. Bazzacco, P. Bednarczyk, B. Birkenbach, D. Bortolato, et al., Nucl. Instrum. Methods Phys. Res., Sect. A **638**(1), 96 (2011)
19. S. Akkoyun, et al., Nucl. Instrum. Methods Phys. Res., Sect. A **668**, 26 (2012). DOI https://doi.org/10.1016/j.nima.2011.11.081. URL https://www.sciencedirect.com/science/article/pii/S0168900211021516

20. M. Deleplanque, I. Lee, K. Vetter, G. Schmid, F. Stephens, R. Clark, R. Diamond, P. Fallon, A. Macchiavelli, Nucl. Instrum. Methods Phys. Res., Sect. A **430**(2), 292 (1999). DOI https://doi.org/10.1016/S0168-9002(99)00187-4. URL https://www.sciencedirect.com/science/article/pii/S0168900299001874
21. S. Paschalis, I. Lee, A. Macchiavelli, C. Campbell, M. Cromaz, S. Gros, J. Pavan, J. Qian, R. Clark, H. Crawford, et al., Nucl. Instrum. Methods Phys. Res., Sect. A **709**, 44 (2013)
22. D. Weisshaar, D. Bazin, P. Bender, C. Campbell, F. Recchia, V. Bader, T. Baugher, J. Belarge, M. Carpenter, H. Crawford, M. Cromaz, B. Elman, P. Fallon, A. Forney, A. Gade, J. Harker, N. Kobayashi, C. Langer, T. Lauritsen, I. Lee, A. Lemasson, B. Longfellow, E. Lunderberg, A. Macchiavelli, K. Miki, S. Momiyama, S. Noji, D. Radford, M. Scott, J. Sethi, S. Stroberg, C. Sullivan, R. Titus, A. Wiens, S. Williams, K. Wimmer, S. Zhu, Nucl. Instrum. Methods Phys. Res., Sect. A **847**, 187 (2017). DOI https://doi.org/10.1016/j.nima.2016.12.001. URL https://www.sciencedirect.com/science/article/pii/S0168900216312402
23. A. Korichi, T. Lauritsen, Eur. Phys. J. A **55**(7), 121 (2019)
24. S. Heil, S. Paschalis, M. Petri, The European Physical Journal A **54**(10), 172 (2018)
25. R. Venturelli, et al., INFN-LNL Ann. Rep. **204**, 220 (2004)
26. B. Bruyneel, B. Birkenbach, P. Reiter, Eur. Phys. J. A **52**(3), 70 (2016)
27. M. Labiche, J. Ljungvall, F. Crespi, S. Chen, J. Bordes, A. Goasduff, S. Bottoni, E. Gamba, R. Pérez-Vidal, M. Bentley, Eur. Phys. J. A **59**(7), 158 (2023)
28. Agata repository. URL https://gitlab.com/malabi-agata/agata
29. S. Agostinelli, et al., Nucl. Instrum. Methods Phys. Res., Sect. A **506**(3), 250 (2003). DOI http://dx.doi.org/10.1016/S0168-9002(03)01368-8. URL http://www.sciencedirect.com/science/article/pii/S0168900203013688
30. J. Allison, et al., Nucl. Instrum. Methods Phys. Res., Sect. A **835**, 186 (2016). DOI https://doi.org/10.1016/j.nima.2016.06.125. URL https://www.sciencedirect.com/science/article/pii/S0168900216306957
31. J. Ljungvall, Eur. Phys. J. A **57**(6), 198 (2021)
32. A. Lopez-Martens, K. Hauschild, A. Korichi, J. Roccaz, J.P. Thibaud, Nucl. Instrum. Methods Phys. Res., Sect. A **533**(3), 454 (2004). DOI https://doi.org/10.1016/j.nima.2004.06.154. URL https://www.sciencedirect.com/science/article/pii/S0168900204014779
33. M. Siciliano, J. Ljungvall, A. Goasduff, A. Lopez-Martens, M. Zielińska, AGATA, O. collaborations, Eur. Phys. J. A **57**(2), 64 (2021)
34. F. Recchia, D. Bazzacco, E. Farnea, A. Gadea, R. Venturelli, T. Beck, P. Bednarczyk, A. Buerger, A. Dewald, M. Dimmock, et al., Nucl. Instrum. Methods Phys. Res., Sect. A **604**(3), 555 (2009)